Journal of Volcanology and Geothermal Research 439 (2023) 107840

Contents lists available at ScienceDirect

Journal of Volcanology and Geothermal Research

journal homepage: www.journals.elsevier.com/journal-of-volcanology-and-geothermal-research

# Crater morphology, nested ring structures, and temperature anomalies studied by unoccupied aircraft system data at Lascar volcano, northern Chile

Lun Ai [a,*], Thomas R. Walter [a], Felipe Aguilera [b,c,d], Susana Layana [b,c], René Mania [a], Christian Kujawa [a], Martin Zimmer [a], Manuel Inostroza [b]

[a] GFZ German Research Center for Geosciences, Telegrafenberg, Potsdam, Germany
[b] Millennium Institute on Volcanic Risk Research-Ckelar Volcanoes, Antofagasta, Chile
[c] Centro de Investigación para la Gestión Integrada del Riesgo de Desastres (CIGIDEN), Santiago, Chile
[d] Departamento de Ciencias Geológicas, Univerisdad Católica del Norte, Antofagasta, Chile

ARTICLE INFO

*Keywords:*
Lascar volcano
UAS
Crater geomorphology
Ring structure
Volcanic conduit

ABSTRACT

Details of ongoing changes in geomorphology and structure of nested volcanic craters are lacking due to the difficult and hazardous access. In this study, we present a novel unoccupied aircraft system (UAS) dataset collected at Lascar, northern Chile, one of the most active volcanoes in the Central Volcanic Zone of the Andes. Lascar features nested craters, the deepest crater of which has experienced repeated lava dome emplacement and numerous violent explosions in recent decades. We performed UAS surveys in 2017 and 2020 to collect the optical and thermal imaging data of the active crater. By applying the Structure-from-Motion (SfM) method, we obtained centimeter-scale optical and thermal orthomosaics as well as digital terrain models. We quantify the spatial and volumetric changes that occurred during the observation period. The results show material removal from the crater wall and a significant accumulation of volcanic material on the crater floor. The thermal orthomosaic helps identify thermal anomalies and the spatial distribution of fumaroles. The highest thermal anomaly was found on the crater floor and delimited by ring structures. Both the optical orthomosaics and DEMs from 2017 and 2020 showed a consistent ring structure, which remained stable following two explosive events. Possible localized subsidence was observed within the ring structure. Consequently, we hypothesize that the ring structure represents the surface expression of underlying concentric fracture systems and constrains a narrow conduit top. Our results provide important insights into an active crater's morphological, structural, and thermal features, with implications for understanding the formation mechanism and evolution of volcanic craters.

## 1. Introduction

Volcanic craters are bowl or funnel-shaped morphological depressions commonly located at the top of a volcanic cone. Volcanic craters can be formed by explosive excavation, ejection of country rock, and constructive accumulation of eruptive material around a vent during explosions (Branney and Acocella, 2015). Volcanic craters often surround smaller secondary vents, forming an overlapping or nested architecture common in arc stratovolcanoes. The formation mechanism of nested craters is usually associated with vent migration (Lipman, 1997), gravitational movement of volcanic material (de Zeeuw-van Dalfsen et al., 2017), and alternatively, subsidence of a crater floor accommodated by concentric fractures (Matthews et al., 1997).

Prominent examples of a nested appearance can be observed at Telica in Nicaragua, which hosts two partially overlapping craters (Hanagan et al., 2020), and Turrialba in Costa Rica, which shows at least three linearly trending craters (Martini et al., 2010). Many nested craters also host ephemeral lava domes, such as Colima and Popocatépetl in Mexico (Robin et al., 1991; Gómez-Vazquez et al., 2016), and Sabancaya in Peru (Gerbe and Thouret, 2004). These volcanoes pose a significant hazard as they can lead to explosive eruptions, dome or flank collapses, and generate high eruption columns and pyroclastic density currents

*Abbreviations:* UAS, unoccupied aircraft system.

* Corresponding author.
*E-mail address:* ailun@gfz-potsdam.de (L. Ai).

https://doi.org/10.1016/j.jvolgeores.2023.107840
Received 29 August 2022; Received in revised form 27 May 2023; Accepted 6 June 2023
Available online 14 June 2023

(Calder et al., 2015). Such destructive behavior was demonstrated by the 1993 sub-Plinian eruption of the Lascar volcano in northern Chile, which contains five partially overlapping and nested craters, and a lava dome was emplaced within the currently active crater (Gardeweg and Medina, 1994; Matthews et al., 1997).

Understanding the dimension and formation of nested volcanic craters is essential. Crater diameter can be used to estimate the energy of an explosion and assess potential hazards (Taddeucci et al., 2010; Valentine et al., 2012). Lava dome emplacement is also thought to be related to the nested appearance (Matthews et al., 1997). Changes in crater morphology and hydrothermal activity are highly relevant even during periods of quiescence, and monitoring their changes is crucial for predicting volcanic unrest. Unfortunately, Lascar's active summit crater is partially hidden from satellite monitoring and ground survey, such as LiDAR measurements, due to steep slopes and shadow effects (de Zeeuw-van Dalfsen et al., 2017). Direct field observations of the elevated crater are difficult and hazardous to access, especially during periods of activity. High-resolution remote sensing surveys such as airplanes and helicopters are expensive for conducting multiple tasks. Crucial details of the thermal features, such as localized fumaroles are challenging to determine on low-resolution infrared satellite data (Francis and Rothery, 1987; Glaze et al., 1989; Oppenheimer et al., 1993; Wooster and Rothery, 1997; Denniss et al., 1998; Wooster, 2001; Blackett, 2013).

Small commercial unoccupied aircraft systems (UAS), also known as drones, have become a viable alternative for monitoring these high-elevation regions. UAS are low-cost and have enhanced flight capabilities to reach altitudes of more than 1 km while carrying high-resolution optical and thermal imaging cameras. This allows for various geophysical measurements and in situ sampling of volcanic gas, ash, and other loose volcanic materials (Jordan, 2019; James et al., 2020). The flexible flight-steering of a UAS allows them to enter near-vent areas or even descend into the crater to acquire data on the inaccessible areas. In some cases, UAS are superior to other satellite or aerial surveys (Turner et al., 2017).

Utilizing the photogrammetric technique of Structure-from-Motion (SfM), ortho maps, point clouds, and topographic models can be reconstructed from a series of photographs (James and Robson, 2012; Westoby et al., 2012). This approach is able to quantify the topographic changes in active craters with a high spatio-temporal resolution, as demonstrated at Stromboli in Italy (Civico et al., 2021) and Telica in Nicaragua (Hanagan et al., 2020). Structural features such as fractures can be mapped on the lava dome within the summit crater of Merapi in Indonesia (Darmawan et al., 2018), and active faults and surface fissures on Mt. Etna in Italy (Tibaldi et al., 2021). In addition, the SfM method can be applied to thermal infrared images to analyze thermal anomalies related to structural and morphologic controls, such as at Ebeko in the Kuril Islands (Walter et al., 2020), and to determine fumarole expression with associated hydrothermal alteration at La Fossa cone in Italy (Müller et al., 2021).

Accordingly, we conducted UAS surveys in 2017 and 2020 at Lascar volcano, with particular emphasis on the active crater. We generated a novel optical, thermal, and topographic dataset at unprecedented levels of spatial resolution. Our data spanned two weak eruptions, allowing us to investigate associated changes. In this work, we illustrated the hidden active crater's detailed morphological, structural, and thermal characteristics. We were able to quantify topographic changes deep within the crater between 2017 and 2020 and determine the location of thermal anomalies and fumaroles. Furthermore, we observed ring structures on the crater floor that may provide valuable insight into the dimensions of the underlying conduit and possible crater formation mechanisms.

## 2. Study area

### 2.1. Geologic background

The composite stratovolcano Lascar (23°22'S, 67°44'W; 5592 m a.s.l.) is located east of the Salar de Atacama basin in northern Chile (Fig. 1a). Lascar belongs to the Central Volcanic Zone of the Andes (CVZ, 14°S-27°S), where magmatism is caused by the subduction of the oceanic Nazca Plate at a rate of 7–9 cm/yr beneath the western margin of the continental South American Plate along the Peru–Chile Trench (de Silva, 1989; Matthews et al., 1994; Stern, 2004). The slab subducts at dips ranging from 10° to 25° and reaches depths of 40–50 km (Contreras-Reyes et al., 2012) and can be traced geophysically to a depth of approximately 400 km (Dorbath et al., 1996).

Lascar comprises two truncated cones, a dormant western cone, and an active eastern cone. The western cone contains two overlapping craters, while the eastern cone has three nested craters (Fig. 1a). The eastern and western cones were built successively as a result of the westward migration of magmatic activity during the early evolutionary stage of Lascar (<220 ka to ~26.5 ka; Gardeweg et al., 1998). The largest explosive eruption identified at Lascar was the Soncor eruption (~26.5 ka), which produced 10–15 $km^3$ of pyroclastic flows, widespread pumice deposits, and ignimbrite sheets extending 27 km west of the volcano (Gardeweg et al., 1998). A silicic stratocone was later formed over the Soncor eruption site, now preserved as two overlapping craters on the western cone (Gardeweg et al., 1998; Matthews et al., 1999; Calder et al., 2000). After the Tumbres eruption (~9.3 ka), the activity migrated back to the eastern cone and produced the Tumbres-Talabre andesitic lava flow (~7.1 ka), which extended 8 km to the northwest (Fig. 1a; Gardeweg et al., 1998). The Tumbres-Talabre lava flow was cut off by the easternmost of the three nested craters, the western of which is currently active (Matthews et al., 1997; Gardeweg et al., 1998).

### 2.2. Recent volcanic activity

Lascar is one of the most active volcanoes in the CVZ, and its eruptive activity has been reported since historical records in the 1840s (Francis and Rothery, 1987). Volcanic activity since 1984 has been characterized by cyclic behavior, beginning with the emplacement of a lava dome within the western crater and ending with a major explosive eruption (Matthews et al., 1997; Gardeweg et al., 1998). The subsidence of the lava dome was typically accompanied by frequent minor explosions (Matthews et al., 1997). The largest recent activity occurred during the sub-Plinian eruption (VEI 4) of 19–20 April 1993 (Gardeweg and Medina, 1994). The 1993 eruption produced a 23 km high plume, extensive ash fallouts, and pumice-rich pyroclastic flows with an estimated volume of 0.02 $km^3$ that spread 8 km to the northwest and 4 km to the southeast (Fig. 1a; Sparks et al., 1997; Jessop et al., 2012; Calder et al., 2000). Following the 1993 eruption, an andesitic lava dome was emplaced within the western crater and extended outwards to occupy part of the southern crater terrace (Matthews et al., 1997). This lava dome was almost four times larger than its predecessors, reaching a diameter of 380 m and a volume of $4.6 \times 10^6$ $m^3$ (Global Volcanism Program, 1993). The cyclic behavior of Lascar ended after the 1993 eruption, the lava dome began to subside and was gradually removed by accompanying minor explosions (Matthews et al., 1997).

Volcanic activity after the 1993 eruption was dominated by persistent fumarolic emissions, short-lived Vulcanian or phreatic explosions of varying intensity, and gas or ash plumes reaching a few kilometers above the summit (Aguilera et al., 2006; Menard et al., 2014; González et al., 2015; Gaete et al., 2020). After a 6-year quiescence from 2007 to 2013, volcanic activity resumed with an eruption in April 2013 (Layana et al., 2020). The most recent explosive event took place on 30 October 2015, producing an ash plume that rose 2.5 km above the summit (Gaete et al., 2020). Other small explosions were detected on 30 November 2018 and 11 September 2019 based on optical and thermal satellite data, which were accompanied by a rapid increase in the thermal anomaly followed by a gradual decrease (see Supplementary Material).

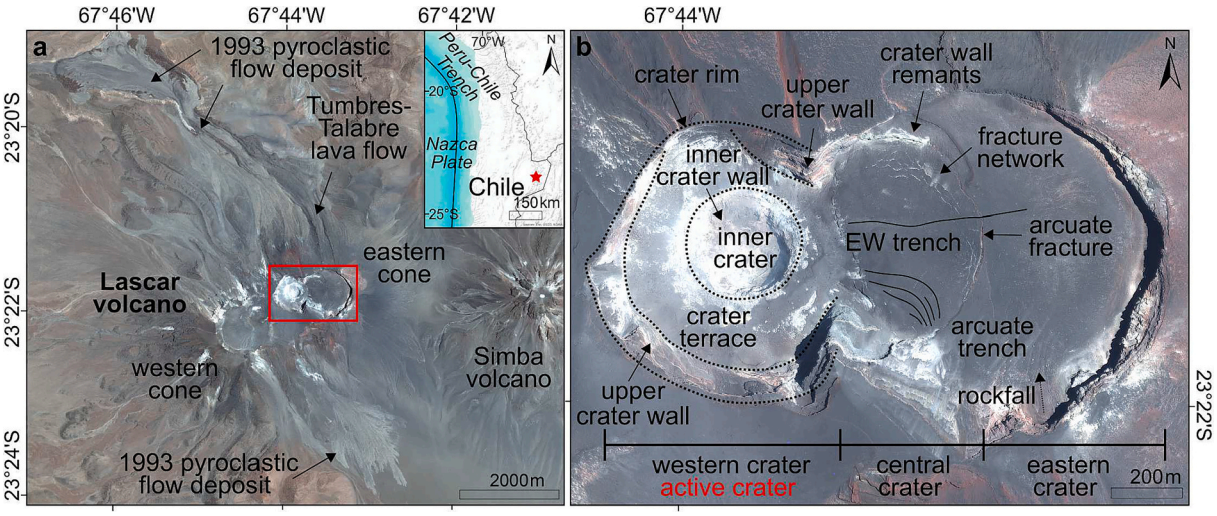


**Fig. 1.** Study area and the nested crater. (a) Location of Lascar volcano in northern Chile (red star in the inset). The large map of the pan-sharpened Pléiades-1A satellite image (acquired on 22 November 2016), shows the elongated edifices in a SW-NE direction and predominant deposits from previous eruptions of Lascar. (b) The close-up view of the eastern cone highlights its three nested craters, named the western, central, and eastern craters. The boundaries of the upper crater wall, the crater terrace, and the inner crater wall are marked by black dashed lines.

### 2.3. Crater formation and ongoing changes

The three nested craters are referred to as the western, central, and eastern craters, respectively (Fig. 1b). Remnants of the central crater wall can be seen to the north, while other parts are buried by pyroclastic deposits predominantly produced during the 1993 eruption (Sparks et al., 1997; Jessop et al., 2012). A westward-opening arcuate fracture defines the possible structural limit and separates the eastern crater from the central crater. The western crater cross-cuts the central crater and has been the site of eruptions in the past decades (Fig. 1b).

The formation and dynamics of the three nested craters at Lascar remain debated. Due to the absence of evident deposits relevant to significant explosive events, their formation could not be explained by caldera-forming collapse or conventional crater formation mechanisms (Matthews et al., 1997; Gardeweg et al., 1998). Alternatively, Matthews et al. (1997) proposed a partially gas-driven and cyclic subsidence mechanism. According to this view, degassing of a lava dome and underlying magma reduces the volume and initiates subsidence of the lava dome. Hydrothermal alteration decreases permeability, further inhibiting gas loss and increasing gas pressure in the upper conduit system, which may lead to explosive eruptions (Heap et al., 2019). Repeated dome emplacement and eruptions result in piston-like subsidence of the crater floor, eventually forming the present nested feature at Lascar (Matthews et al., 1997). Intense hydrothermal activity is well observed on Lascar's summit, as seen in many other volcanoes, which would explain not only crater formation but also episodic unrest. According to sandbox analog experiments, de Zeeuw-van Dalfsen et al. (2017) suggest that the central crater appeared as a parasitic structure between two pre-existing craters, resulting from gravitational slumping of material towards the western crater caused by its deepening.

The relationship between Lascar's nested craters and their underlying conduits and its magmatic plumbing system is still unclear. Deformation measurements have been used to detect local subsidence at a millimeter scale between 1993–2000 (Pavez et al., 2006) and 2012–2017 (Richter et al., 2018). However, no evidence of volcano-wide surface deformation was found during the eruptions of Lascar, especially during the major eruption in 1993 (Pritchard and Simons, 2002; Pritchard and Simons, 2004). This suggests the absence of shallow magma chambers, but rather a narrow and vertical conduit identified in seismic experiments (Gaete et al., 2019). Local subsidence has been interpreted as gravitational movement and compaction of eruptive deposits within the crater (Richter et al., 2018). A comparable magnitude of subsidence has been observed on pumice flow deposits from the 1993 eruption. This has been linked to post-emplacement processes such as thermal contraction and gravitational compaction (Whelley et al., 2012). The occurrence of an E-W trending trench and fracture networks on the central crater surface (Fig. 1b) may also be explained by post-emplacement subsidence. Minor subsidence has been observed on the upper northern and southeastern crater terraces, likely due to gravitational processes (Richter et al., 2018). Despite attempts to determine and monitor the structure and dynamics of the inner crater, these were unsuccessful until unoccupied aircraft system (UAS) surveys at high altitudes became feasible, as described below.

## 3. Data and methods

### 3.1. UAS survey in 2017 and 2020

Repeated unoccupied aircraft system (UAS) surveys were performed on 27 November 2017 and 25 February 2020. UAS flights were realized from the southern rim (67°43'50"W, 23°21'1"S; 5499 m a.s.l.) of the western crater (launch sites and flight paths are shown in Fig. 2a and b). We used different types of quadcopters for the surveys. In 2017, we employed a DJI Mavic Pro Platinum carrying a 1/2.3-inch CMOS camera sensor with a resolution of 4000 × 3000 pixels. The UAS transmitted 455 nadir view images during the flight before it crashed. In 2020, we used two UASs, a DJI Phantom 4 RTK and a DJI Mavic 2. The Phantom 4 and Mavic 2 were equipped with 1-inch CMOS sensors providing improved position accuracy and an image resolution of 5472 × 3648 pixels. The DJI Mavic 2 successfully descended approximately 220 m into the inner crater to capture close-range nadir and oblique images. In total, we obtained 1257 optical nadir/near-nadir and oblique images during the 2020 overflights.

Additionally, the Phantom 4 carried a FLIR Tau 2 640 thermal imaging camera (13 mm lens) attached to a ThermalCapture 2.0 frame grabber. The thermal camera recorded radiometric images at wavebands between 7.5 and 13.5 μm at a sampling rate of 8 Hz and were geotagged by a GPS antenna. The radiometric temperature was recorded directly with a thermal resolution of 0.04 degrees and an image resolution of 640 × 512 pixels. The thermal camera was calibrated for a temperature range of −25 °C to +135 °C and 1315 thermal infrared images were acquired.

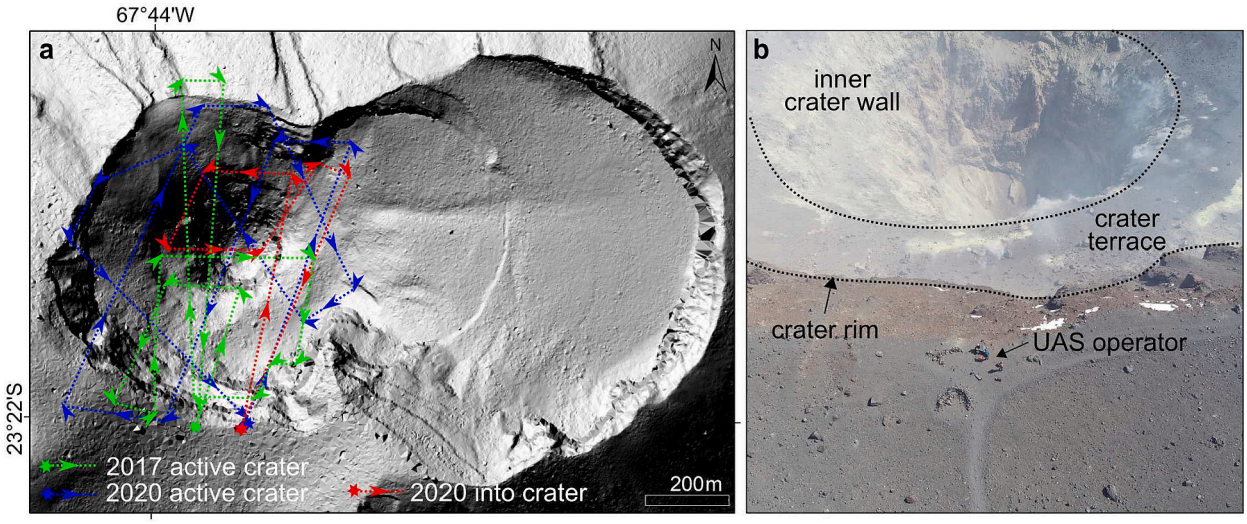


**Fig. 2.** Unoccupied aircraft system (UAS) survey. (a) UAS launch location (colored star) and flight path (dashed line with arrow) are shown on a shaded relief map. (b) The UAS image shows the launch location close to the crater rim.

### 3.2. Structure-from-Motion (SfM) processing

We use Agisoft Metashape (version 1.7.3) to process the optical UAS images. The software utilizes a Structure-from-Motion (SfM) and Multi-View-Stereo (MVS) approach to construct a high-precision orthomosaic and 3D topographic model. Ground Control Points (GCPs) were not available within Lascar's active crater, position accuracy relied on camera orientation parameters, on-board global navigation satellite system (GNSS) geotagging, and real-time kinematic (RTK) correction. UAS images containing large areas of cloud and gas were manually deleted to ensure image quality. To reduce the within-model error, we selected 15–20 reference objects, such as stationary blocks or cliff edges, to define check points in Agisoft. We also calculated the point confidence of a point cloud, with lower confidence values assuming higher uncertainties. Points with very low confidence values (1–2) and isolated floating points were removed to enhance the reliability of the results.

We designated the 2020 point cloud (phantom RTK) as the reference and registered the 2017 point cloud to the 2020 point cloud. This was achieved by selecting 9 GCPs that were distributed on the crater terrace from the 2020 dataset. Consequently, we obtained a relative root-mean-square error (RMSE) of 0.23 m between the 2017 and 2020 point clouds. Optical orthomosaics and digital elevation models (DEMs) were created for the 2017 and 2020 datasets. Both the 2017 and 2020 orthomosaics showed a large area of shadow on the crater floor, the UAS flight descending into the inner crater was shadow-free and provided higher resolution. We created an additional orthomosaic in Agisoft using these data, georeferenced it to the 2020 dataset, and replaced the central crater area of the 2020 orthomosaic in ArcMap (version 10.8).

The photogrammetric processing of the thermal infrared images was conducted using the Pix4Dmapper software (v4.5.6), which is a commercial software also based on the SfM algorithm. The raw radiometric data were first calibrated in ThermoViewer software (v3.0.7). We assumed a constant emissivity of 0.95 for a typical volcanic environment (Stevenson and Varley, 2008), a transmissivity of 0.7, an environmental and path temperature of 10 °C, and a humidity of 10% (Menard et al., 2014). The radiometric data were exported in a 24-bit RGB RJPG image format, which contains complete radiometric information and is compatible with the Pix4Dmapper solver. Pix4Dmapper was found to yield improved alignment results (1138 out of 1315 images, ~87%) compared to Agisoft Metashape (<50%). The output thermal orthomosaic has a spatial resolution of 45 cm/pixel and a radiometric resolution of 0.04 degree/pixel, which allowed us to identify fumaroles and blocks on the crater terrace and use them as GCPs. To integrate the thermal data with the optical data, we georeferenced the thermal orthomosaic to the 2020 optical orthomosaic in ArcMap (version 10.8).

### 3.3. DEM of Difference analysis

DEM of Difference (DoD) analysis allows us to estimate the vertical distance between two digital elevation models on a cell-by-cell basis (James et al., 2012) and quantify topographic and volumetric changes. To ensure consistency, we resampled the 2017 and 2020 DEMs to a uniform resolution of 0.15 m and defined an identical spatial extent. We perform the DoD analysis using Geomorphic Change Detection (GCD) in ArcGIS (GCD add-in, version 7.5.0.0, http://gcd.riverscapes.xyz/). We consider the geomorphic changes to be reliable if they are greater than the inherent uncertainties of the DEM (Wheaton et al., 2010; James and Robson, 2012). Therefore, we applied the minimum level of detection method, where the threshold can be estimated from the root mean square error (RMSE) between the component DEMs (Milan et al., 2007). The relative RMSE between the 2017 and 2020 DEMs was calculated to be 0.23 m. However, we note that systematic errors or artifacts increase towards the DEM boundary, especially in the 2017 DEM, which shows obvious curvature deformation on the upper northern terrace. To minimize the impact of systematic errors, we increased the minimum level of detection threshold to 1 m. As a result, we obtained a thresholded map of elevation changes and the minimum area and volume difference.

## 4. Results

The Structure-from-Motion (SfM) approach enables the construction of a high-precision dataset that includes (1) optical orthomosaics for 2017 and 2020 with resolutions of 7.7 and 7.0 cm/pixel, respectively; (2) an orthomosaic for 2020 with a resolution of 5.3 cm/pixel that replaces the central crater area; (3) DEMs for 2017 and 2020 with resolutions of 15.6 and 13.7 cm, respectively; and (4) a thermal orthomosaic for 2020 with a spatial resolution of 45.0 cm/pixel and a radiometric resolution of 0.04 degree/pixel. This comprehensive and high-quality representation of the study area, allows us to accurately analyze the geomorphology and structure of the hidden inner crater, identify the distribution of thermal anomalies and fumaroles, and quantify the topographic changes that occurred between November 2017 and February 2020.

### 4.1. General overview

The western crater is enclosed by nearly cylindrical upper crater walls (~5499 m a.s.l.) that are open to the east where they intersect with the central crater (Fig. 3b). The western crater has an approximate area of $3.9 \times 10^5$ m$^2$. The inner crater is positioned at the center and is surrounded by the crater terrace. The inner crater has a diameter of 310 m (N-S) to 340 m (W-E), with an area of $9.1 \times 10^4$ m$^2$ and a volume of $6.7 \times 10^6$ m$^3$. The inner crater walls are asymmetrical, with the north and west walls sloping at an angle of 45°-60°, while the south and east walls are nearly 90° (Fig. 3f). The crater floor (lowest point ~5076 m a.s.l.) is bounded by the inner crater wall and covers an area of $2.08 \times 10^4$ m$^2$. The southern crater terrace rises 170 m above the crater floor and slopes inwards by 10°-30°, with the northwest terrace being steeper than the southeast side (Fig. 3f). Rockfalls originating from the west to south upper crater walls are deposited on the terrace, while those on the western terrace tend to slide further into the inner crater (Fig. 3b). Besides rockfalls, numerous large boulders, some exceeding 2–3 m in diameter, are distributed across the terrace. Several shallow erosion channels, known as furrows, are visible on the northern terrace, measuring about 2–3 m wide and half a meter deep (Fig. 3b).

### 4.2. Fumarole and hydrothermal alteration expression

The joint analysis of optical and thermal infrared data enable the detection of fumaroles and associated hydrothermal alteration zones. The fumarolic activity shown in the optical image is dominated by white steam, accordingly, we identified 46 steaming sites in 2017 and 76 steaming sites in 2020 based on the optical data (Fig. 3d and e). Note that the visibility of steaming can be significantly affected by meteorological conditions (see Discussion). The thermal orthomosaic covers the inner crater and a part of the terrace (Fig. 3c). Thermal anomalies are identified as apparent temperatures above the background temperature (38 °C), and local temperature peaks represent fumarolic activity (see Supplementary Material). With the help of the thermal mosaic, we further identified 131 fumaroles in 2020 (Fig. 3f).

Prominent fumaroles are distributed on the upper level of the inner crater wall and on the southern terrace (Fig. 3d and e), characterized by vigorous white to translucent steam and surrounded by yellowish sulfur deposits and whitish alteration aureoles. Their apparent temperatures range from around 40 °C to 150 °C. Other fumaroles are scattered across the middle part of the inner crater wall, and many of them discharge from isolated cracks with few fumarolic deposits and lower apparent temperatures (around 38 °C to 70 °C) and steam intensity. The whitish to

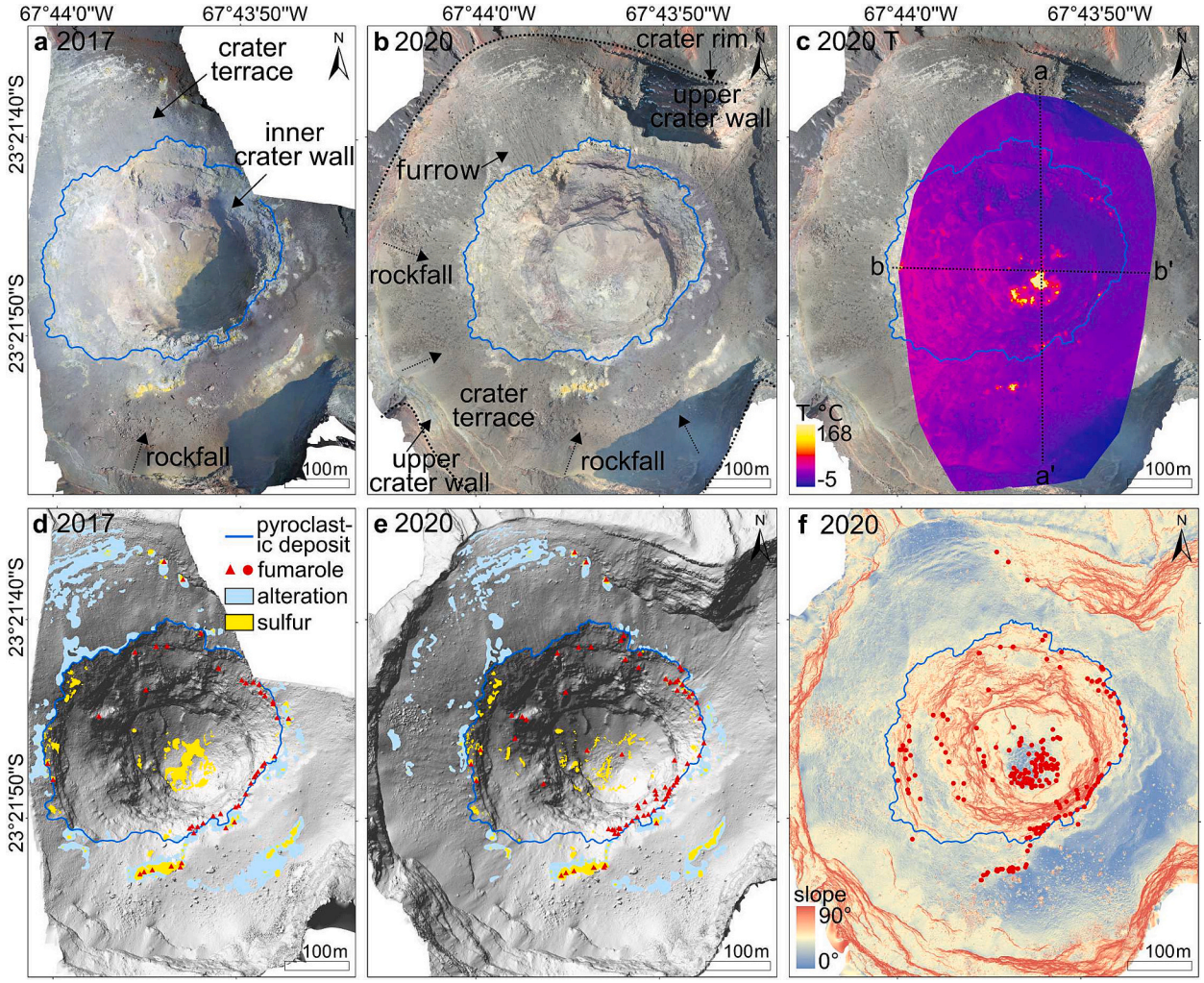


**Fig. 3.** Overview of the optical and thermal orthomosaics. (a) The 2017 optical orthomosaic. The blue line indicates the boundary between the inner crater wall and the pyroclastic deposits. (b) The 2020 optical orthomosaic, where the central area has been replaced by a higher resolution orthomosaic. (c) The thermal orthomosaic of 2020, which measures the apparent temperature range from −5 °C to 168 °C. Black dashed lines indicate the topographic and temperature profiles are shown in Fig. 6. (d) and (e) Hillshademaps of 2017 and 2020 with identified sulfur deposits (yellow) and hydrothermal alteration zones (light blue). Red triangles indicate visible steam. (f) The 2020 slope map, with fumaroles (red dots) distinguished from the thermal mosaic.

grayish hydrothermal alteration zones are readily distinguishable from the dark gray pyroclastic deposits on the terrace surface (Fig. 3a and b). We note that hydrothermal alteration is virtually absent on the inner crater wall, where lava and pyroclastic material are exposed. Therefore, we highlight the boundary between the exposed crater walls and the pyroclastic deposits on the terrace (Fig. 3). Most of the alteration is devoid of visible steam, except for a cluster of fumaroles situated on the upper northern terrace, which displays weak steam in both years (Fig. 3d and e).

The highest and largest thermal anomalies are found on the crater floor, where the highest apparent temperatures exceed 168 °C (Fig. 3 and enclose an area of approximately $4.5 \times 10^3$ m$^2$. The position and extent of the thermal anomaly on the crater floor derived from the UAS data are consistent with the values obtained from the satellite thermal image (on 23 February 2020, see Supplementary Material). The latter has 13 pixels on the SWIR image (band 11), which is equivalent to an area of $5.2 \times 10^3$ m$^2$. Significant fumarolic deposits are present on the central crater floor but exhibit weak steam activity.

### 4.3. Inner crater wall and crater floor morphology

Observation of the steep inner crater wall is limited by the nadir UAS view and the final product orthomosaic. Therefore, we utilized oblique photos acquired during the 2020 UAS survey. The UAS image shows that the lower part of the inner crater wall is constituted of massive lava blocks (Fig. 4a), likely remnants of the earlier lava dome. The lava blocks are overlain by diverse pyroclastic deposits with localized fumarolic materials (Fig. 4b). Numerous erosional gullies are present on the west wall about 30–60 m long and 3–10 m deep (black dashed arrows in Fig. 4a), as well as collapse structures on the north wall (8–12 m in diameter; red dashed lines in Fig. 4b). Tension cracks on the northeast wall are associated with slope instability (Fig. 4c). Notably, the inner crater wall is virtually absent of any radial or other-oriented dike or sill intrusion.

The crater floor is covered with angular screes and fumarolic deposits (Fig. 5a and d). A comparison between the 2017 and 2020 orthomosaics shows that the primary lithological features have remained stable (see structural lines in Fig. 5a and d). Several debris talus fans have newly developed on the northwest to the northeast crater floor, and the number of large angular clasts (up to 3 m in diameter) in the central crater floor has significantly increased in the 2020 orthomosaic (Fig. 5b and e). Correspondingly, the yellowish sulfur deposits have reduced in area due to overlying volcanic materials from 2017 to 2020 (Fig. 5b and e). Despite the changes in the deposits on the crater floor, a fracture-like arcuate feature oriented in a NE-SW direction (about 40 m long) appears in the same position in both the 2017 and 2020 orthomosaics (red line with teeth in Fig. 5b and e).

We identified a nested ring structure on the crater floor by analyzing slope maps generated from the 2017 and 2020 DEMs (labeled rings a, b, and c in Fig. 5c and f). Ring a (~90 m in diameter) is represented by lithological elements in the north and arcuate lithological features in the south where the kink in the slope is located. Ring b (~40 m in diameter) is represented by the arcuate fracture in the northwest and extends concentrically. Ring b hosts several smaller ring-like structures, one of which is highlighted as ring c (~16 m in diameter). The position of the ring structure is decentralized, with rings b and c forming concentric circles that are offset to the southeast (Fig. 5c and f). At locations where the apparent temperature exceeds 150 °C, the fumarolic deposits exhibit a dark brown and "wet" appearance, likely representing liquid sulfur, which is predominantly enclosed by rings b and c (Fig. 5e and f).

### 4.4. Morphological changes from 2017 to 2020

#### 4.4.1. DEM and thermal profiles

According to the N-S and W-E topographic profiles, changes have occurred predominantly on the crater floor, where the 2020 profile overlays the 2017 profile (Fig. 6a and b). The maximum positive value (indicating material addition) along both the N-S and W-E profiles on the crater floor is 3.7 m. It should be noted that the profiles may not exactly cross the location of maximum material addition. The south and east inner crater walls, in turn, exhibit significant negative values (-32 m in the N-S profile and −17 m in the W-E profile). We treat these large DEM difference values with caution as they occurred on the near vertical sections, and no corresponding large mass loss was found on oblique UAS photos at the same location. The large negative values are likely to represent errors, which could be the result of mispositioning during point cloud alignment or included in the DEM error (see Discussion).

Apparent temperature profiles allow thermal anomalies to be correlated with topography. Our analysis reveals that fumaroles are mainly located at kinks in the slope where the crater terrace transitions into the steep inner crater wall. The apparent temperature of these fumaroles is nearly two times lower than that of the fumaroles on the crater floor. Moreover, we observed that the western section of the inner crater is exposed to direct sunlight and is about 20 °C higher than the

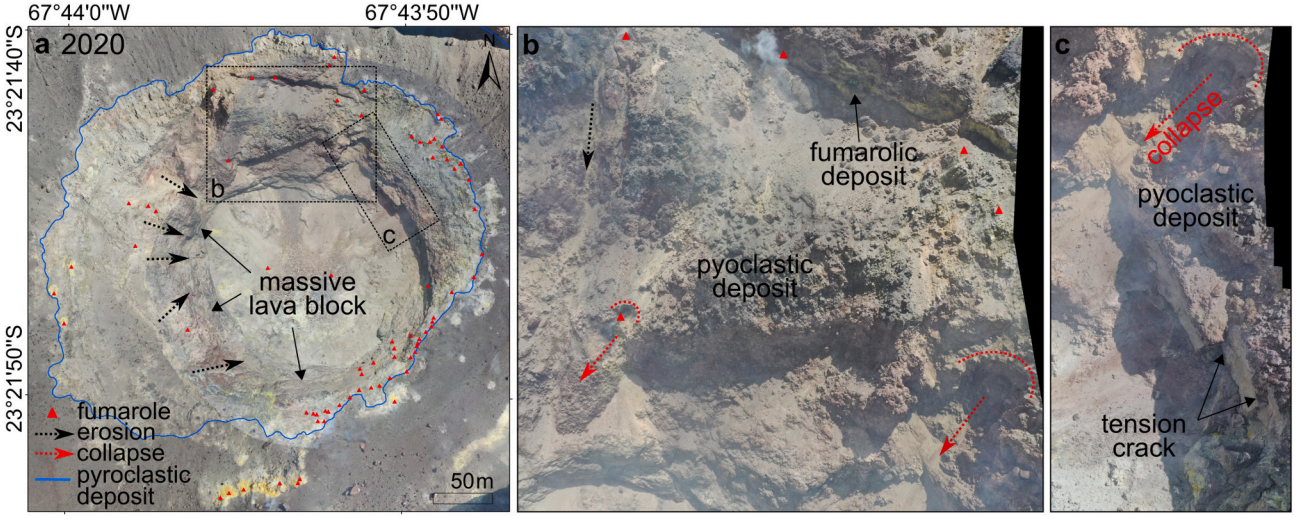


**Fig. 4.** Inner crater wall morphology. (a) A close-up view of the inner crater from the 2020 orthomosaic. The inset box indicates the location of oblique UAS photos. Eroded gullies carving the west wall are indicated by black dashed arrows. (b) Agglomerated pyroclastic onlaps and half-circle collapse holes on the north wall. (c) Localized fractures on the northeast wall indicate ongoing collapse.

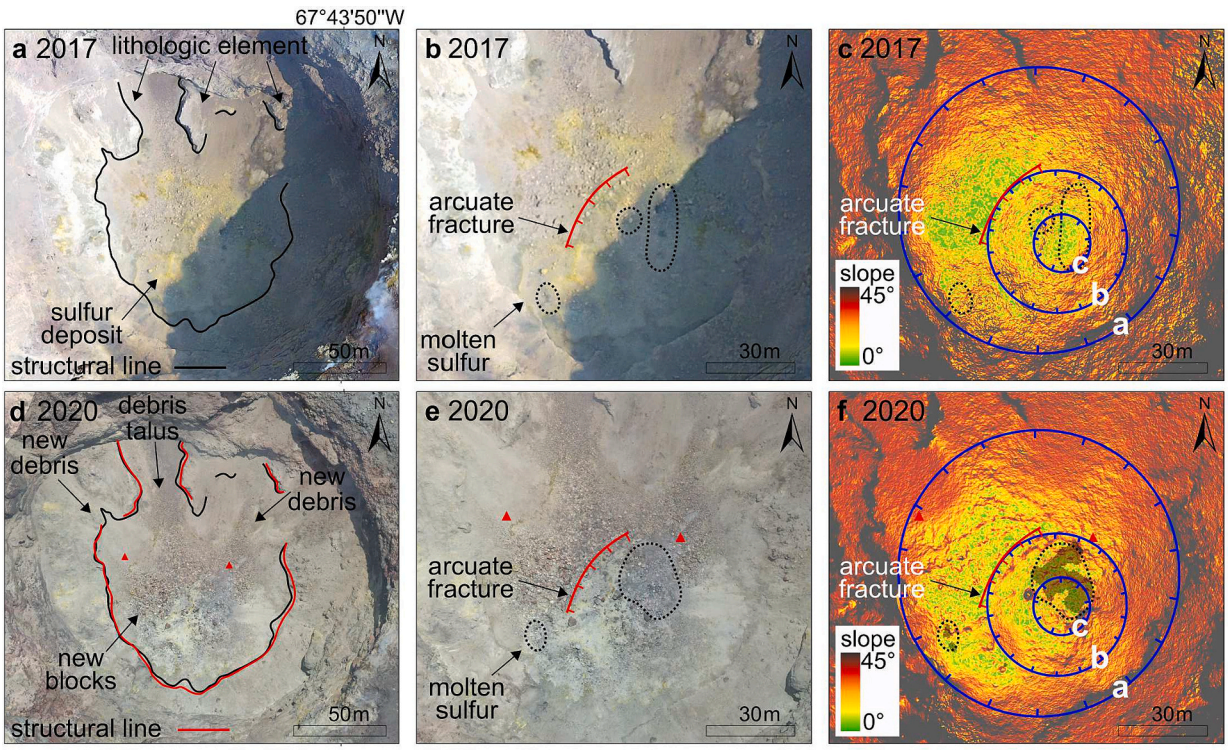


**Fig. 5.** Crater floor morphology and ring structure. (a) The 2017 orthomosaic shows the outlines of lithological elements on the crater floor (black line). (b) A close-up view of the 2017 orthomosaic highlights an arcuate fracture (red line). Liquid sulfur deposits are enclosed by black dashed ellipses. (c) The 2017 slope map illustrates ring structures labeled a, b, and c. (d) The 2020 orthomosaic shows a comparison of the lithological outlines of 2017 (black) and 2020 (red). (e) A close-up view of the 2020 orthomosaic, red triangles indicate visible steam. (f) The 2020 slope map shows ring structures. Gray shading represents apparent temperatures above 150 °C.

shaded eastern part (Fig. 6b). Similarly, piles of rocks and other volcanic materials on the crater floor reduce the apparent temperature by at least 20 °C (Fig. 6a).

#### 4.4.2. *DEM of Difference (DoD) analysis*

Comparison of the orthomosaics and DEM profiles suggests that topographic changes are predominantly concentrated on the crater floor, whereas the crater terrace has remained unchanged. To better visualize and quantify these subtle variations, we created an elevation change map based on the DoD analysis (Fig. 7a). As a result, 92.91% of the area was stable, mainly the crater terrace, which is represented by gray bars on the histogram (Fig. 7c and d). The results show positive and negative values in the elevation change map, representing material gain and loss, respectively (Fig. 7a).

The DoD analysis shows that the area of material gain is $1.13 \times 10^4$ $m^2$ (74.11%), while the area of material loss is $0.39 \times 10^4$ $m^2$ (25.98%). The volume of material gain accounts for $2.02 \times 10^4$ $m^3$ (61.92%) and the volume of material loss for $1.24 \times 10^4$ $m^3$ (38.08%). The total volume of material gain is greater than the material loss by a factor of 1.6. The dominant area of material gain is identified at the crater floor, where newly deposited volcanic material has accumulated up to 6.85 m, corresponding to a volume gain of $1.65 \times 10^4$ $m^3$. Material loss occurs primarily on the upper inner crater wall, especially in the northern section. Notably, we identified evident localized removals of large volumes (the largest exceeding 400 $m^3$) on the north wall (Fig. 7b). The locations of material loss are consistent with the half-circle holes observed in oblique UAS images (Fig. 4b and c). Some areas of material gain are inconsistent with optical observations and are considered errors (Fig. 7b), likely due to vertical or overhanging walls (see Discussion).

## 5. Discussion

Repeated UAS surveys were carried out over the active crater of Lascar. Photogrammetric processing provided a high-resolution optical, topographic, and thermal dataset that allowed us to investigate the ongoing changes that have taken place in the hidden crater over the period of 2017 to 2020. Here, we address the limitations and uncertainties arising from the use of UAS and the subsequent data analysis. We examine the redistribution of material in the inner crater, the control of the distribution of fumaroles and associated hydrothermal alteration, the ring structure on the crater floor, and the possible mechanism of crater formation, and compare our findings with nested crater structures elsewhere.

### 5.1. *Limitations and uncertainties*

#### 5.1.1. *Limitations of UAS survey and image quality*

Environmental conditions posed the main challenge for our UAS surveys, especially at high altitudes such as the Lascar summit crater (over 5500 m a.s.l.). The stability of UAS flights is strongly affected by wind velocity. Low air pressure and strong winds often lead to maximum rotor speed and cause the UAS to drift leeward. In addition, gusty and turbulent winds can cause the UAS to flip over, particularly during takeoff and landing. We also experienced electronic malfunctions, such as remote control and stabilization failures, which we believe were related to the high-altitude exposure. Later UAS testing at lower altitudes did not replicate these malfunctions. Low temperatures can rapidly drain lithium batteries. As a precaution, we replaced the battery when its capacity dropped to 30%.

The quality of the acquired images was dependent on several factors, including camera calibration, motion blur, and light source. The presence of vigorous fumarolic degassing in the active volcanic crater area

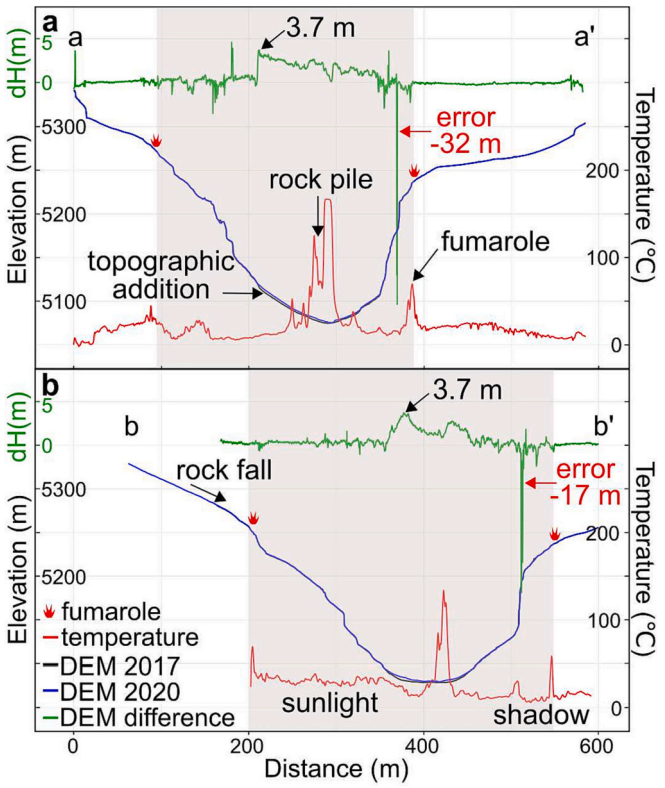


**Fig. 6.** DEM and thermal profiles. The location of the profiles is shown in Fig. 3c. (a) N-S profiles (a-a') of the 2017 DEM (black line), the 2020 DEM (blue line), the DEM difference (green line; obtained by subtracting the 2017 DEM from the 2020 DEM and exaggerated by a factor of 10 for better visualization), and the 2020 apparent temperature (red line). The gray shaded box outlines the approximate extent of the inner crater. (b) W-E profiles (b-b').

obscured the view and caused the camera to be out of focus. Airframe vibration induced by high rotor speeds also contributed to the loss of focus in some instances. The sun's position caused shadow lengths to vary, especially on the crater floor, which affected the image quality and the SfM-derived products. By comparing the 2017 and 2020 optical orthomosaics, we noted changes in the visual appearance of the alteration zone. In 2017, the alteration zone appeared white to light yellow, while in 2020, it appeared white to gray. The aureole of sulfur deposits appeared dark turquoise in 2017 and more yellowish-brownish in 2020. This apparent color discrepancy is possibly attributed to changing light conditions and camera parameters. The surveys used different types of UAS, with the camera employed in 2017 having an exposure value of −1.7, while in 2020, it was 0. Consequently, images from 2017 had an overall higher color saturation than images from 2020. Therefore, assessments based on optical orthomosaics should be taken with caution.

### 5.1.2. *Limitations of thermal infrared measurement*

Thermal radiometric measurements are influenced by numerous environmental and technical factors. These factors include surface conditions, target object emissivity and reflectivity, instrument viewing angle, and air path length. Environmental conditions such as solar reflectance, air particulate, atmospheric transmission, and relative humidity also play an important role (Ball and Pinkerton, 2006; Chiodini et al., 2007; Spampinato et al., 2011). Fuming plumes, steam condensation, and long air paths lead to signal absorption. For instance, in our case, approximately 250 m flight height over the southern crater terrace resulted in large pixel sizes and an underestimation of the apparent temperature (Harris et al., 2009).

Although the thermal orthomosaic can achieve a spatial resolution of 45 cm/pixel, the diameter of fumarole vents determined from optical orthomosaics is typically less than 45 cm. Moreover, the thermal mosaic displays a pixel-integrated temperature that contains a hot vent surrounded by a cooler background, resulting in an apparent temperature that is lower than the actual temperature of the fumaroles (Harris and Stevenson, 1997; Harris et al., 2009). The temperature of fumaroles is influenced by meteorological conditions such as precipitation and atmospheric pressure (Zimmer et al., 2017). In this context, it should be noted that the number of fumaroles identified in our study represents only a relative amount rather than the real number. Nevertheless, the spatial distribution of fumaroles is still valid, as the fumarole fields are depicted by distinct thermal anomalies.

The thermal radiometric survey utilized the high gain mode of the FLIR Tau sensor, which has an upper-temperature detection limit calibrated and set at 135 °C. However, the measured maximum apparent temperature of 165 °C on the crater floor is obviously oversaturated. We believe that the true temperature may exceed these values by a factor of 2 or more. Additionally, shaded areas inside the crater appear to affect the apparent temperature, reducing it by at least 20 °C between shaded and sunlit areas. Therefore, choosing an appropriate time of day to avoid large areas of shadow is essential for achieving an optimal UAS survey.

### 5.1.3. *Photogrammetry uncertainties*

A common issue encountered in photogrammetric processing is the absence of ground control points, especially in active volcanic areas (Hanagan et al., 2020). Position accuracy relies mainly on on-board GNSS geotagging and camera positions. Direct georeferencing without GCPs has proven its feasibility in producing reliable topographic models (Carbonneau and Dietrich, 2017; James et al., 2017). Position uncertainty and its propagation into the SfM products were assessed by Kalacska et al. (2020), which suggests that the position error ranges from <1 m to >3 m depending on the type of GNSS employed, while the SfM within-model error without GCPs was <0.3 m. However, the assessment was conducted under ideal conditions, and the position error may increase significantly in high-altitude areas due to the loss of satellite signal. Instead of georeferencing to an absolute position, we registered the UAS-derived datasets relative to each other, using the Phantom RTK point cloud as a reference and corresponding objects as control points. While relative positioning has a minor impact on morphological change studies, it necessitates the cautious selection of control points without significant morphological variation.

Both the 2017 and 2020 models show enhanced systematic errors towards the model boundaries. In particular, the 2017 point cloud yields a curvature artifact on the northern upper terrace which is not present in the 2020 point cloud. This artifact may be attributed to low overlap and coverage of acquired images, as well as the poor camera quality of the UAS used in 2017. To mitigate such artifacts, rigorous calibration of the camera model, increased image coverage and overlap, and the inclusion of oblique images and well-distributed ground control points are required (James and Robson, 2014; Griffiths and Burningham, 2019). As our UAS crashed into the crater in 2017, the available camera records cannot be further corrected. Therefore, the aforementioned limitations should be taken into account in future UAS survey designs.

We applied a minimum level of detection with a threshold of 1 m during the DEM of difference (DoD) analysis, which allowed us to exclude the region affected by systematic errors. This subjectively chosen threshold ensures the accuracy and reliability of the DoD results, which are essential for this study. However, the DoD analysis is limited to 2.5D surfaces with reduced resolution compared to 3D point clouds, and subtle details of morphological changes are neglected. Furthermore, the vertical surface cannot be described by a DEM, and DoD may lose validity on near-vertical or overhanging crater walls (Lague et al., 2013; James et al., 2017). Inherent DEM uncertainties arising from data acquisition, point cloud registration, interpolation, and other factors are unavoidable (James et al., 2012), and inherent uncertainties will propagate into the DoD analysis, ultimately enhancing the uncertainty in the final output (Brasington et al., 2003).

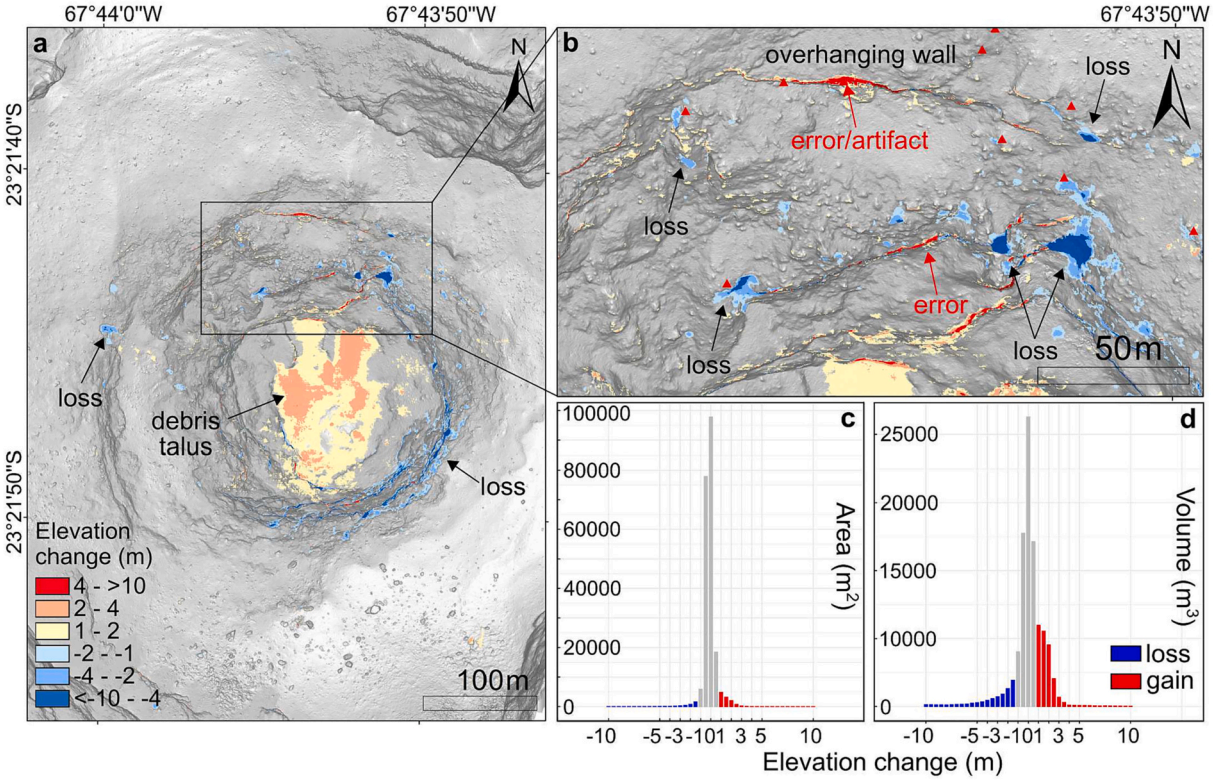


**Fig. 7.** DEM of difference analysis. (a) The elevation change map is superimposed on the hillshade map of 2020. Positive values indicate material gain, while negative values indicate material loss. (b) A close-up view of the northern section shows large volume losses (blue shading), errors or artifacts (red arrow), and fumarole sites (red triangle). (c) and (d) Histograms of areal and volumetric changes based on thresholded DEM difference. The gray bar represents the value below the threshold of the minimum level of detection (1 m). The red and blue bars represent material gain and loss, respectively. Notably, the histograms demonstrate a net gain in area and volume.

### 5.2. Fumarole and hydrothermal alteration control

The spatial distribution of fumaroles can be controlled by different mechanisms, including the stress field, lithology, and permeability contrasts (such as fractures, faults, and shear bands). The stress field in elevated regions can promote fluid ascent, leading to the preferential distribution of fumaroles and alteration zones in areas of high topography, such as crater rims (Schöpa et al., 2011). At Lascar, prominent high-temperature fumaroles (>100 °C in our study) are primarily concentrated on the uppermost inner crater wall, contributing to the extensive gas output. According to historical records (Oppenheimer et al., 1993; Matthews et al., 1997; Tassi et al., 2009), most of these fumaroles are likely long-lived, having been fed directly by subsurface magma (before 2006) and more recently influenced by the shallow hydrothermal system (Tassi et al., 2009; Menard et al., 2014).

Isolated fumaroles distributed in the middle to lower parts of the inner crater wall appear at lower temperatures and activity levels. Similar spatial distributions of fumaroles are observed on Vulcano Island in Italy (Schöpa et al., 2011; Spampinato et al., 2011; Müller et al., 2021), and Bezymianny in Russia (Carter et al., 2007). Fumaroles and surrounding alteration zones on the south to the southeast terrace of Lascar are arranged concentrically and coincide with the extent of the 1993 lava dome (Matthews et al., 1997). Of particular note is that these fumaroles first appeared following the subsidence/collapse of the 1993 lava dome (Global Volcanism Program, 1994). This implies a possible structural control related to fractures that developed during dome subsidence or even earlier during the dome emplacement stage. Fumaroles distributed along the periphery of a lava dome are commonly observed at the volcanic summit crater, as seen at Colima volcano in Mexico (Salzer et al., 2017) and Santiaguito in Guatemala (Sahetapy-Engel and Harris, 2009). Fumaroles may indicate localized tensile failure associated with gravitational sliding, such as the cluster of fumaroles and stripped hydrothermal alteration zones on the steep upper northern terrace of Lascar.

### 5.3. Material redistribution on the crater floor

From November 2017 to February 2020, a total of $2.02 \times 10^4$ m$^3$ of volcanic material was added to the crater floor. These deposits may have a variety of origins. First, collapse, rockfalls, and gravitational landslides from the inner crater wall, as evidenced by oblique UAS observations and DoD analysis. Some collapses are found in areas where localized fumarolic activity is present. Similar scenarios have been observed at Telica in Nicaragua, where persistent fumarolic activity has resulted in hydrothermal alteration and promoted crater wall weakening and collapse (Hanagan et al., 2020). At Merapi in Indonesia, fumaroles and alteration regions in 2015 rapidly developed into a deep scar in 2017 (Darmawan et al., 2022). Second, rockfalls and landslides are sourced from the upper crater wall. The steep northwest terrace appears to be a source of landslides, as evidenced by tensile fractures and deformation measurements (Richter et al., 2018). Third, material originating from eruptive activity, such as ejected materials falling and rolling back into the inner crater (Valentine et al., 2012) during minor explosions in November 2018 and September 2019 (see Supplementary Material), and/or new lava extrusion may have contributed to the addition of volcanic material.

Notably, the total volume gain on the crater floor is $0.41 \times 10^4$ m$^3$, greater than the total volume loss on the inner crater walls. The following possibilities could explain this apparent discrepancy. First, systematic and photogrammetric errors (see Section 5.1). Second, material from regions not included in the DoD analysis, such as the upper crater wall. Third, the crater floor was uplifted by magmatic processes.

Previous geodetic studies could not detect deformation with respect to magmatic intrusions, and coherent data were not available for the deep inner crater (Pritchard and Simons, 2002; Pritchard and Simons, 2004; Pavez et al., 2006; Richter et al., 2018). We speculate that any deformation, if present, may have been confined to the crater floor and on a small scale. Optical satellite images from November and December 2018 reveal a dark circle in the central crater floor, accompanied by a sharp increase in thermal anomalies (see Supplementary Material). This dark circle may represent the presence of new lava or liquid sulfur deposits. However, changes in surface texture occur rapidly on the crater floor and are difficult to distinguish from low-resolution satellite data.

### 5.4. Ring structures on the crater floor

The slope maps and orthomosaics of 2017 and 2020 exhibit strong similarities in the identified ring structures (Fig. 8a and b), despite the fact that two explosions occurred between two UAS surveys which may have triggered the deposition and/or redeposition of materials on the crater floor. As shown in the 2017 slope map (Fig. 8b), the area enclosed by ring b shows multiple concentric features encircling a flat area within ring c, whereas the same area within ring c is marked by a more pronounced inward-dipping slope in the 2020 slope map (Fig. 8e). This implies that subsidence may have occurred within the ring c; however, no obvious vertical displacement of the ring structures was observed. Instead, the DoD map indicates an overall uplift of the crater floor (Fig. 8a). Nevertheless, we noted that most of the deposited material is in the region of ring a, with less material in ring b (<1–2 m) and ring c (<1 m) (Fig. 8a). This is inconsistent with the optical orthomosaics, which show a significant increase in the number of clasts within ring b and ring c (Fig. 8c and f). The arcuate fracture representing the segment boundary of ring b has remained stable (Fig. 8c and f). The above observations suggest that subsidence has occurred in the center of ring c and along the edge of ring b (arcuate fracture), with an estimated subsidence magnitude of less than 1–2 m.

Shear zones associated with lava dome extrusions are known to represent heterogeneities in rheology and permeability (Heap et al., 2016). While the permeability of extruding lava may be relatively homogeneous, the marginal shear zones exhibit significant heterogeneity, which may control the escape of volatiles and temperature expression (Gaunt et al., 2014). Concentric heterogeneities are thought to control the explosivity and formation of extruding lava domes and spines (Walter et al., 2022). In the case of Lascar volcano, a comparison of the ring structures with the thermal orthomosaic indicates that the ring structure exactly confines the highest apparent temperature (Fig. 8d and e). Fumaroles at the edges of the ring structures, such as in rings a and b, imply the existence of fractures or high permeability at the crater floor. This provides compelling evidence of heterogeneity resulting from a ring fracture system that delineates a degassing underlying conduit. The ring fracture system was believed to be active during the period of the UAS survey.

### 5.5. Conceptual model of the ring structure

The driving mechanism of ring structures is a critical question that pertains to the nested summit crater of Lascar and other volcanoes. Ring structures may provide valuable insights into the conduit geometry and pathways of heat and mass, and contribute to the development of heterogeneities relevant to fluid flow and deformation transients. Ring faults are commonly associated with caldera collapse caused by magma chamber deflation (Lipman, 2000; Roche et al., 2000). Based on analog experiments, outward-dipping reverse faults initiate at the margins of the magma chamber and propagate upward, whereas inward-dipping normal faults develop subsequently at the periphery near the surface and propagate downward. Eventually, the peripheral normal faults join with the reverse faults at depth (Burchardt and Walter, 2010). Similar ring faults develop on a smaller scale during pit crater collapse, where

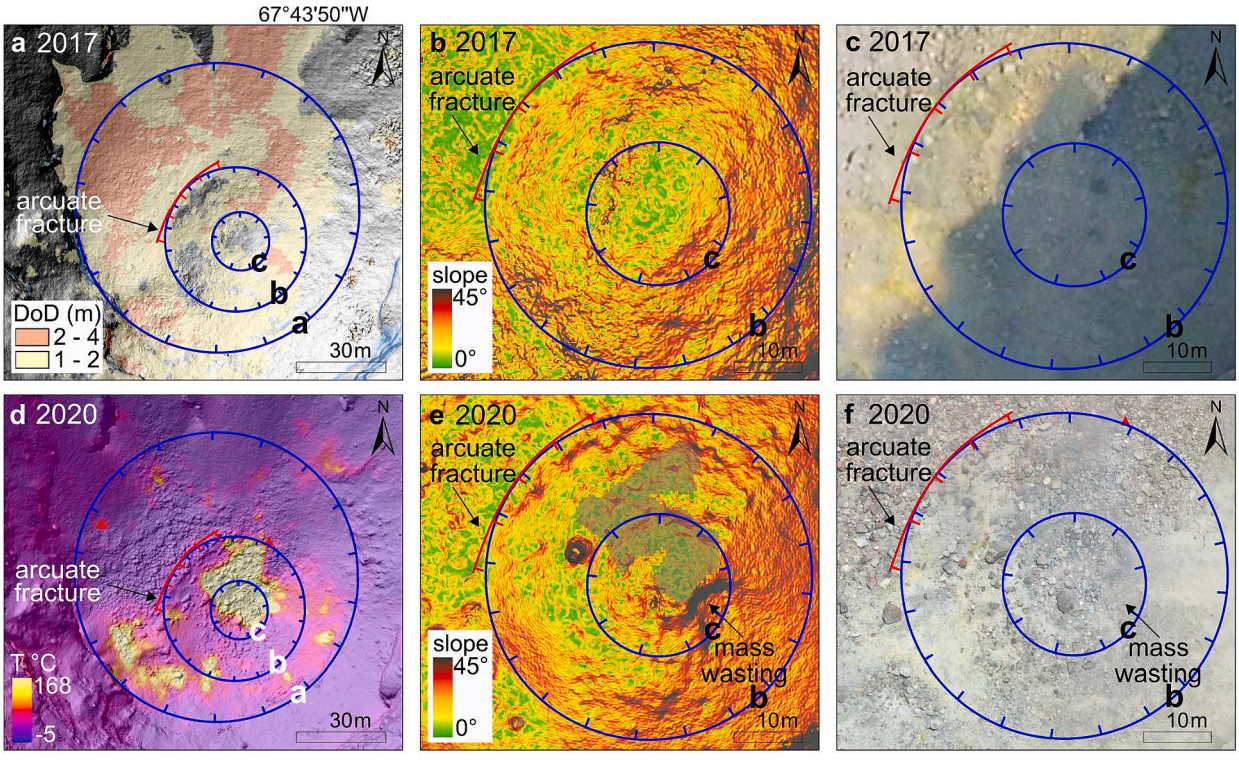


**Fig. 8.** Nested ring structures on the crater floor. (a) The DEM of Difference map overlaid on the 2017 hillshade map, note that the lower amount of deposition inside ring b. (b) A close-up view of rings b and c in the 2017 slope map. (c) The 2017 orthomosaic reveals an evident arcuate fracture. (d) The thermal orthomosaic overlaid on the 2020 hillshade map. (e) A close-up view of rings b and c in the 2020 slope map. Gray shading represents apparent temperatures in excess of 150 °C. (f) The 2020 orthomosaic shows an identical arcuate fracture as 2017.

subsidence is manifested as a coherent piston collapse (Roche et al., 2001). Outward-dipping reverse faults appear initially on the periphery, and subsidence occurs along these reverse faults, triggering the formation of inward-dipping normal faults, which subsequently join together at depth. Such collapse-characterized subsidence has been widely observed, such as at Miyakejima in Japan (Geshi et al., 2002; Burchardt and Walter, 2010) and Masaya in Nicaragua (Roche et al., 2001; Harris, 2009).

The above studies only consider subsidence mechanisms, ring faults may also form or be reactivated during extrusion from the same conduit. In an experiment simulating lava dome and spine extrusion, upwardly divergent thrust faults evolve with dome growth, while vertical faults form during lava extrusion (Zorn et al., 2020; Walter et al., 2022). Observing an internal or subsurface ring fault system in a natural lava dome is challenging. Nevertheless, ring fractures on the dome surface have been observed at Santiaguito in Guatemala (Bluth and Rose, 2004; Sahetapy-Engel and Harris, 2009). These ring fractures are composed of relatively cooler inner rings and hotter outer rings, corresponding to the lava plug in the central conduit surrounded by ring-fractured shear zones at the conduit margin. The thermal pattern of ring structures on the crater floor of Lascar is different from that observed at Santiaguito volcano, where hot inner rings (rings b and c) and a cooler outer ring (ring a) are expressed (Fig. 8d).

According to Matthews et al. (1997), concentric fractures developed on the dome surface during extrusion, and subsequent dome subsidence was accommodated by inward-stepped ring fracture systems, where the ring fractures behaved as normal faults. The growth of the lava dome cannot be reconstructed from the data we present; however, our UAS observations support the subsidence mechanism. As we noted, the overall crater floor rose due to deposition, while possible localized subsidence occurs within ring b. The stability of the ring structures during explosive events suggests a deeper control. The ring structures are likely the surface expression of a subsurface fracture system.

Hence, we speculate that the ring structure appears as a consequence of the interplay of two structural processes: extrusion and subsidence along ring fractures. Growth and reactivation of ring fractures result in geometrically well-constrained thermal emissions. As ring structures are linked to the underlying source, their extension may provide a preliminary estimation of the dimensions of the underlying conduit. Therefore, we propose a conceptual model of ring structures (Fig. 9a and b), where the outer ring (ring a) is a normal fault (NF) that dips inward, and the inner ring (ring b) features a vertical to outward-dipping reverse fault (RF). The ring fractures eventually merge to the main conduit margin at depth. Consequently, we constrain a narrow underlying conduit that does not exceed 40 m in diameter (the extent of ring b). The estimated dimensions of the ring structure appear small but agree with observations at other volcanoes, such as Santiaguito, where diameters of 70 m have been determined (Bluth and Rose, 2004; Holland et al., 2011). Vulcanian to Plinian eruptions may occur at narrow conduits with diameters of 10–20 m (Burgisser and Degruyter, 2015).

During the early stages of dome building and collapse, the formation of the nested western crater was dominated by a subsidence mechanism (Matthews et al., 1997). Our findings suggest that subsidence of the crater floor may be continuing at a small scale, and ongoing gravitational collapse and widening play a greater role in the current deep crater shape. The UAS-based investigation of the ring structure at Lascar is essential to better understand the conduit geometry and its stability during periods of quiescence and degassing. Our interpretations are mainly based on the coherent caldera roof and pit crater collapse, and spine extrusion, further experimental and modeling studies are required to verify our hypothesis. In addition, new activity began in late 2022, culminating in an eruption on 10 December 2022 and the extrusion of a lava dome in the inner crater on January 2023 (Global Volcanism Program, 2023). The structural changes caused by this new activity may provide valuable insights into the persistence of ring structures during eruptive periods.

## 6. Conclusion

Repeat UAS surveys were realized at the active crater of Lascar in 2017 and 2020, and acquired optical and thermal infrared images. By utilizing the Structure-from-Motion (SfM) method, we generated optical and thermal orthomosaics as well as topographic models at a scale of 5–45 cm. This comprehensive high-resolution dataset allowed us to map the hidden inner crater's detailed morphological, structural, and thermal features. By calculating the difference between the 2017 and 2020 DEMs, we quantified the topographic changes that occurred during this period. We observed a large number of localized material removal on the inner crater wall ($1.24 \times 10^4$ m$^3$) and a significant accumulation of volcanic deposits on the crater floor, reaching a thickness of 6.85 m and a volume of $1.65 \times 10^4$ m$^3$. With the help of the thermal orthomosaic, we identified that fumarole activity is primarily concentrated at the upper level of the inner crater wall and the crater floor. The highest thermal anomaly was found on the crater floor and delimited by ring structures. These ring structures show remarkable consistency in both the 2017 and 2020 optical orthomosaics and DEMs, and remained stable after the two explosive events. Our findings enable us to conceptualize that the ring structure possibly represents subsurface fracture systems,

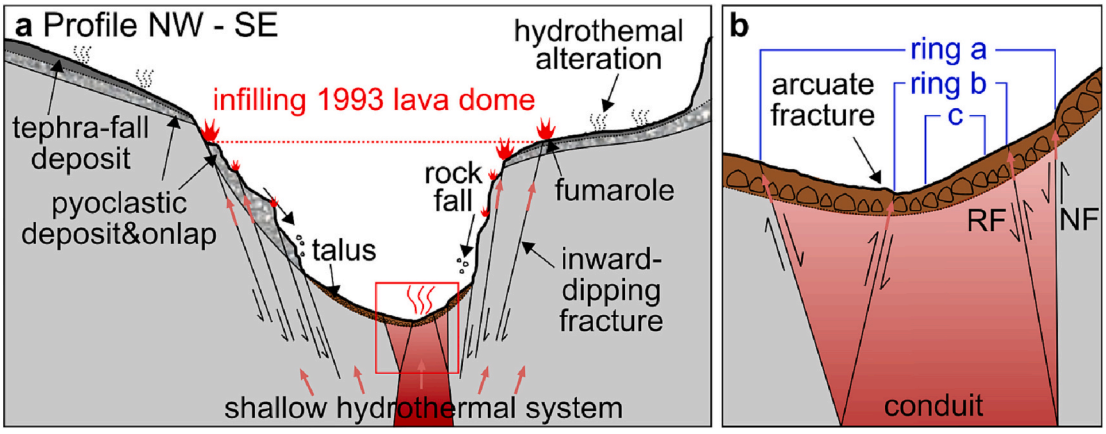


**Fig. 9.** Conceptual model of the ring structure. (a) Schematic NW to SE profile illustrates the funnel and asymmetrical shape of the inner crater, the distribution of fumaroles and diverse pyroclastic deposits, the ongoing collapse of the inner crater wall, and deposition on the crater floor. The red dashed line approximates the level of the 1993 lava dome. The inner crater is accommodated by an inward-dipping fracture system (modified after Matthews et al., 1997) and ring structures on the crater floor. The heat may follow the fracture and reach the surface. (b) A close-up view of the ring structures highlights ring a representing the normal fault (NF) and ring b representing the reverse fault (RF), where subsidence occurred within ring b.

which are formed by the interaction between extrusion/deposition and subsidence of volcanic materials along the ring structure. The dimension of ring structures implies the geometry of a narrow conduit top not exceeding 40 m. Thus, our study successfully demonstrated the application of UAS to an active volcanic crater. Emphasizing the ongoing changes in the crater morphology could help better understand crater formation and evolution, thereby providing critical insights for predicting future behavior.

## Authors contribution

L.A. processed and analyzed the data, and led the writing and conceptualization of the manuscript. T.R.W. supervised the project and field work, and contributed to the writing and conceptualization of the manuscript. F.A. contributed to the understanding of general volcanological descriptions. C.K., R.M., M.Z., and M.I. contributed to the field work, C.K. and R.M. conducted the drone flights in 2017 and 2020. S.L. studied satellite thermal imagery. All authors contributed to drafting and revising the manuscript.

## Declaration of Competing Interest

The authors declare that they have no known competing financial interests or personal relationships that could have appeared to influence the work reported in this paper.

## Data availability

The UAS data is available at https://doi.org/10.5281/zenodo.7538045.

## Acknowledgements

This is a contribution to the IPOC (Integrated Plate Boundary Observatory Chile), a European-South American network of institutions and scientists that organizes and operates a distributed system of instruments and projects dedicated to the study of earthquakes and deformation at the continental margin of Chile. A.L. acknowledges financial support from the China Scholarship Council (Grant No. 202008080293). Financial support for T.R.W. and R.M. comes from the ERC-CoG VOLCAPSE (project ID646858). S.L. is funded by CONICYT-PCHA Doctorado Nacional fellowship (2016–21160276). S.L., F.A, and M.I. were partially funded by the Antofagasta Regional Government (FIC-R project, code BIP N°30488832–0). S.L. and F.A. were partially funded by the Research Center for Integrated Disaster Risk Management (CIGIDEN, ANID/FONDAP/15110017).

## Appendix A. Supplementary data

Supplementary data associated with this article can be found, in the online version, at https://doi.org/10.1016/j.jvolgeores.2023.107840 and at https://doi.org/10.5281/zenodo.7538045.

## References

Aguilera, F., Viramonte, J., Medina, E., Guzmán, K., Becchio, R., Granados, H.D., Arnosio, M., 2006. Recent eruptive activity from Lascar volcano (2003–2005). In: 11th Chilean Geological Congress. Universidad Católica del Norte, Antofagasta, pp. 397–400.

Ball, M., Pinkerton, H., 2006. Factors affecting the accuracy of thermal imaging cameras in volcanology. J. Geophys. Res.: Solid Earth 111, 1–14. https://doi.org/10.1029/2005JB003829.

Blackett, M., 2013. Review of the utility of infrared remote sensing for detecting and monitoring volcanic activity with the case study of shortwave infrared data for Lascar Volcano from 2001–2005. Geol. Soc. Spec. Pub. 380, 107–135. https://doi.org/10.1144/SP380.10.

Bluth, G.J., Rose, W.I., 2004. Observations of eruptive activity at santiaguito volcano, guatemala. J. Volcanol. Geoth. Res. 136, 297–302. https://doi.org/10.1016/j.jvolgeores.2004.06.001.

Branney, M., Acocella, V., 2015. Calderas. In: Sigurdsson, H. (Ed.), The Encyclopedia of Volcanoes, Second ed. Academic Press, pp. 299–315. https://doi.org/10.1016/B978-0-12-385938-9.00016-X.

Brasington, J., Langham, J., Rumsby, B., 2003. Methodological sensitivity of morphometric estimates of coarse fluvial sediment transport. Geomorphology 53, 299–316. https://doi.org/10.1016/S0169-555X(02)00320-3.

Burchardt, S., Walter, T.R., 2010. Propagation, linkage, and interaction of caldera ring-faults: Comparison between analogue experiments and caldera collapse at Miyakejima, Japan, in 2000. Bull. Volcanol. 72, 297–308. https://doi.org/10.1007/s00445-009-0321-7.

Burgisser, A., Degruyter, W., 2015. Magma ascent and degassing at shallow levels. In: Sigurdsson, H. (Ed.), The Encyclopedia of Volcanoes, Second ed. Academic Press, pp. 225–236. https://doi.org/10.1016/B978-0-12-385938-9.00011-0.

Calder, E.S., Lavallée, Y., Kendrick, J.E., Bernstein, M., 2015. Lava Dome Eruptions. In: Sigurdsson, H. (Ed.), The Encyclopedia of Volcanoes, Second ed. Academic Press, pp. 343–362. https://doi.org/10.1016/b978-0-12-385938-9.00018-3.

Calder, E.S., Sparks, R.S.J., Gardeweg, M.C., 2000. Erosion, transport and segregation of pumice and lithic clasts in pyroclastic flows inferred from ignimbrite at Lascar Volcano, Chile. J. Volcanol. Geoth. Res. 104, 201–235. https://doi.org/10.1016/S0377-0273(00)00207-9.

Carbonneau, P.E., Dietrich, J.T., 2017. Cost-effective non-metric photogrammetry from consumer-grade sUAS: implications for direct georeferencing of structure from motion photogrammetry. Earth Surf. Proc. Land. 42, 473–486. https://doi.org/10.1002/esp.4012.

Carter, A.J., Ramsey, M.S., Belousov, A.B., 2007. Detection of a new summit crater on bezymianny volcano lava dome: satellite and field-based thermal data. Bull. Volcanol. 69, 811–815. https://doi.org/10.1007/s00445-007-0113-x.

Chiodini, G., Vilardo, G., Augusti, V., Granieri, D., Caliro, S., Minopoli, C., Terranova, C., 2007. Thermal monitoring of hydrothermal activity by permanent infrared automatic stations: Results obtained at Solfatara di Pozzuoli, Campi Flegrei (Italy). J. Geophys. Res.: Solid Earth 112, 1–13. https://doi.org/10.1029/2007JB005140.

Civico, R., Ricci, T., Scarlato, P., Andronico, D., Cantarero, M., Carr, B.B., Beni, E.D., Bello, E.D., Johnson, J.B., Kueppers, U., Pizzimenti, L., Schmid, M., Strehlow, K., Taddeucci, J., 2021. Unoccupied aircraft systems (UASs) Reveal the Morphological Changes at Stromboli Volcano (Italy) before, between, and after the 3 July and 28 August 2019 Paroxysmal Eruptions. Remote Sens. 13, 2870. https://doi.org/10.3390/rs13152870.

Contreras-Reyes, E., Jara, J., Grevemeyer, I., Ruiz, S., Carrizo, D., 2012. Abrupt change in the dip of the subducting plate beneath north Chile. Nat. Geosci. 5, 342–345. https://doi.org/10.1038/ngeo1447.

Darmawan, H., Troll, V.R., Walter, T.R., Deegan, F.M., Geiger, H., Heap, M.J., Seraphine, N., Harris, C., Humaida, H., Müller, D., 2022. Hidden mechanical weaknesses within lava domes provided by buried high-porosity hydrothermal alteration zones. Sci. Rep. 12, 1–14. https://doi.org/10.1038/s41598-022-06765-9.

Darmawan, H., Walter, T.R., Troll, V.R., Budi-Santoso, A., 2018. Structural weakening of the Merapi dome identified by drone photogrammetry after the 2010 eruption. Nat. Hazards Earth Syst. Sci. 18, 3267–3281. https://doi.org/10.5194/nhess-18-3267-2018.

de Silva, S.L., 1989. Altiplano-Puna volcanic complex of the central Andes. Geology 17, 1102–1106. https://doi.org/10.1130/0091-7613(1989)017<1102:APVCOT>2.3.CO;2.

de Zeeuw-van Dalfsen, E., Richter, N., González, G., Walter, T.R., 2017. Geomorphology and structural development of the nested summit crater of Láscar Volcano studied with Terrestrial Laser Scanner data and analogue modelling. J. Volcanol. Geoth. Res. 329, 1–12. https://doi.org/10.1016/j.jvolgeores.2016.09.018.

Denniss, A.M., Harris, A.J., Rothery, D.A., Francis, P.W., Carlton, R.W., 1998. Satellite observations of the April 1993 eruption of Lascar volcano. Int. J. Remote Sens. 19, 801–821. https://doi.org/10.1080/014311698215739.

Dorbath, C., Paul, A., The Lithoscope Andean Group, 1996. Tomography of the Andean crust and mantle at 20S: first results of the Lithoscope experiment. Phys. Earth Planet. Inter. 97, 133–144. https://doi.org/10.1016/0031-9201(96)03140-8.

Francis, P.W., Rothery, D.A., 1987. Using the Landsat Thematic Mapper to detect and monitor active volcanoes: An example from Lascar volcano, northern Chile. Geology 15, 614–617. https://doi.org/10.1130/0091-7613(1987)15<614:UTLTMT>2.0.CO;2.

Gaete, A., Cesca, S., Franco, L., San Martin, J., Cartes, C., Walter, T.R., 2019. Seismic activity during the 2013–2015 intereruptive phase at Lascar volcano, Chile. Geophys. J. Int. 219, 449–463. https://doi.org/10.1093/gji/ggz297.

Gaete, A., Walter, T.R., Bredemeyer, S., Zimmer, M., Kujawa, C., Franco Marin, L., San Martin, J., Bucarey Parra, C., 2020. Processes culminating in the 2015 phreatic explosion at Lascar volcano, Chile, evidenced by multiparametric data. Nat. Hazards Earth Syst. Sci. 20, 377–397. https://doi.org/10.5194/nhess-20-377-2020.

Gardeweg, M.C., Medina, E., 1994. La erupción subpliniana del 19–20 de Abril de 1993 del Volcan Lascar, N de Chile. In: Acta 7th Congr Geol Chileno, pp. 229–304.

Gardeweg, M.C., Sparks, R.S.J., Matthews, S.J., 1998. Evolution of Lascar Volcano, Northern Chile. J. Geol. Soc. 155, 89–104. https://doi.org/10.1144/gsjgs.155.1.0089.

Gaunt, H.E., Sammonds, P.R., Meredith, P.G., Smith, R., Pallister, J.S., 2014. Pathways for degassing during the lava dome eruption of mount st. helens 2004–2008. Geology 42, 947–950. https://doi.org/10.1130/G35940.1.

Gerbe, M.C., Thouret, J.C., 2004. Role of magma mixing in the petrogenesis of tephra erupted during the 1990–98 explosive activity of Nevado Sabancaya, southern Peru. Bull. Volcanol. 66, 541–561. https://doi.org/10.1007/s00445-004-0340-3.

Geshi, N., Shimano, T., Chiba, T., Nakada, S., 2002. Caldera collapse during the 2000 eruption of miyakejima volcano, japan. Bull. Volcanol. 64, 55–68. https://doi.org/10.1007/s00445-001-0184-z.

Glaze, L.S., Francis, P.W., Self, S., Rothery, D.A., 1989. The 16 September 1986 eruption of Lascar volcano, north Chile: Satellite investigations. Bull. Volcanol. 51, 149–160. https://doi.org/10.1007/BF01067952.

Global Volcanism Program, 1993. Report on Lascar (Chile). In: Wunderman, R. (Ed.), Bulletin of the Global Volcanism Network, 18:11. Smithsonian Institution. https://doi.org/10.5479/si.GVP.BGVN199311-355100.

Global Volcanism Program, 1994. Report on Lascar (Chile). In: Wunderman, R. (Ed.), Bulletin of the Global Volcanism Network, 19:3. Smithsonian Institution. https://doi.org/10.5479/si.GVP.BGVN199403-355100.

Global Volcanism Program, 2023. Report on Lascar (Chile). In: Sennert, S.K. (Ed.), Weekly Volcanic Activity Report, 15 February-21 February 2023. Smithsonian Institution. URL:https://volcano.si.edu/showreport.cfm?wvar=GVP.WVAR20230215-355100.

Gómez-Vazquez, A., De la Cruz-Reyna, S., Mendoza-Rosas, A.T., 2016. The ongoing dome emplacement and destruction cyclic process at Popocatépetl volcano, Central Mexico. Bull. Volcanol. 78 https://doi.org/10.1007/s00445-016-1054-z.

González, C., Inostroza, M., Aguilera, F., González, R., Viramonte, J., Menzies, A., 2015. Heat and mass flux measurements using Landsat images from the 2000–2004 period, Lascar volcano, northern Chile. J. Volcanol. Geoth. Res. 301, 277–292. https://doi.org/10.1016/j.jvolgeores.2015.05.009.

Griffiths, D., Burningham, H., 2019. Comparison of pre-and self-calibrated camera calibration models for uas-derived nadir imagery for a sfm application. Prog. Phys. Geogr.: Earth Environ. 43, 215–235. https://doi.org/10.1177/0309133318788964.

Hanagan, C., La Femina, P.C., Rodgers, M., 2020. Changes in Crater Morphology Associated With Volcanic Activity at Telica Volcano, Nicaragua. Geochem. Geophys. Geosyst. 21, e2019GC008889 https://doi.org/10.1029/2019GC008889.

Harris, A.J., 2009. The pit-craters and pit-crater-filling lavas of masaya volcano. Bull. Volcanol. 71, 541–558. https://doi.org/10.1007/s00445-008-0241-y.

Harris, A.J., Lodato, L., Dehn, J., Spampinato, L., 2009. Thermal characterization of the Vulcano fumarole field. Bull. Volcanol. 71, 441–458. https://doi.org/10.1007/s00445-008-0236-8.

Harris, A.J., Stevenson, D.S., 1997. Thermal observations of degassing open conduits and fumaroles at Stromboli and Vulcano using remotely sensed data. J. Volcanol. Geoth. Res. 76, 175–198. https://doi.org/10.1016/S0377-0273(96)00097-2.

Heap, M., Russell, J., Kennedy, L., 2016. Mechanical behaviour of dacite from mount st. helens (usa): A link between porosity and lava dome extrusion mechanism (dome or spine)? J. Volcanol. Geoth. Res. 328, 159–177. https://doi.org/10.1016/j.jvolgeores.2016.10.015.

Heap, M.J., Troll, V.R., Kushnir, A.R., Gilg, H.A., Collinson, A.S., Deegan, F.M., Darmawan, H., Seraphine, N., Neuberg, J., Walter, T.R., 2019. Hydrothermal alteration of andesitic lava domes can lead to explosive volcanic behaviour. Nat. Commun. 10, 1–10. https://doi.org/10.1038/s41467-019-13102-8.

Holland, A.P., Watson, I.M., Phillips, J.C., Caricchi, L., Dalton, M.P., 2011. Degassing processes during lava dome growth: Insights from santiaguito lava dome, guatemala. J. Volcanol. Geoth. Res. 202, 153–166. https://doi.org/10.1016/j.jvolgeores.2011.02.004.

James, L.A., Hodgson, M.E., Ghoshal, S., Latiolais, M.M., 2012. Geomorphic change detection using historic maps and DEM differencing: The temporal dimension of geospatial analysis. Geomorphology 137, 181–198. https://doi.org/10.1016/j.geomorph.2010.10.039.

James, M.R., Carr, B.B., D'Arcy, F., Diefenbach, A.K., Dietterich, H.R., Fornaciai, A., Lev, E., Liu, E.J., Pieri, D.C., Rodgers, M., Smets, B., Terada, A., von Aulock, F.W., Walter, T.R., Wood, K.T., Zorn, E.U., 2020. Volcanological applications of unoccupied aircraft systems (UAS): Developments, strategies, and future challenges. Volcanica 3, 64–114. https://doi.org/10.30909/vol.03.01.67114.

James, M.R., Robson, S., 2012. Straightforward reconstruction of 3D surfaces and topography with a camera: Accuracy and geoscience application. J. Geophys. Res.: Earth Surf. 117 https://doi.org/10.1029/2011JF002289.

James, M.R., Robson, S., 2014. Mitigating systematic error in topographic models derived from UAV and ground-based image networks. Earth Surf. Proc. Land. 39, 1413–1420. https://doi.org/10.1002/esp.3609.

James, M.R., Robson, S., Smith, M.W., 2017. 3-D uncertainty-based topographic change detection with structure-from-motion photogrammetry: precision maps for ground control and directly georeferenced surveys. Earth Surf. Proc. Land. 42, 1769–1788. https://doi.org/10.1002/esp.4125.

Jessop, D.E., Kelfoun, K., Labazuy, P., Mangeney, A., Roche, O., Tillier, J.L., Trouillet, M., Thibault, G., 2012. LiDAR derived morphology of the 1993 Lascar pyroclastic flow deposits, and implication for flow dynamics and rheology. J. Volcanol. Geoth. Res. 245–246, 81–97. https://doi.org/10.1016/j.jvolgeores.2012.06.030.

Jordan, B.R., 2019. Collecting field data in volcanic landscapes using small UAS (sUAS)/drones. J. Volcanol. Geoth. Res. 385, 231–241. https://doi.org/10.1016/j.jvolgeores.2019.07.006.

Kalacska, M., Lucanus, O., Arroyo-Mora, J.P., Laliberté, É., Elmer, K., Leblanc, G., Groves, A., 2020. Accuracy of 3D Landscape Reconstruction without Ground Control Points Using Different UAS Platforms. Drones 4, 13. https://doi.org/10.3390/drones4020013.

Lague, D., Brodu, N., Leroux, J., 2013. Accurate 3D comparison of complex topography with terrestrial laser scanner: Application to the Rangitikei canyon (NZ). ISPRS J. Photogramm. Remote Sens. 82, 10–26. https://doi.org/10.1016/j.isprsjprs.2013.04.009.

Layana, S., Aguilera, F., Rojo, G., Vergara, Á., Salazar, P., Quispe, J., Urra, P., Urrutia, D., 2020. Volcanic Anomalies Monitoring System (VOLCANOMS), a Low-Cost Volcanic Monitoring System Based on Landsat Images. Remote Sens. 12 https://doi.org/10.3390/rs12101589.

Lipman, P.W., 1997. Subsidence of ash-flow calderas: relation to caldera size and magma-chamber geometry. Bull. Volcanol. 59, 198–218. https://doi.org/10.1007/s004450050186.

Lipman, P.W., 2000. Calderas. In: Encyclopedia of Volcanoes. Academic Press, pp. 643–662.

Martini, F., Tassi, F., Vaselli, O., Del Potro, R., Martinez, M., del Laat Van, R., Fernandez, E., 2010. Geophysical, geochemical and geodetical signals of reawakening at Turrialba volcano (Costa Rica) after almost 150years of quiescence. J. Volcanol. Geoth. Res. 198, 416–432. https://doi.org/10.1016/j.jvolgeores.2010.09.021.

Matthews, S.J., Gardeweg, M.C., Sparks, R.S., 1997. The 1984 to 1996 cyclic activity of Lascar Volcano, northern Chile: cycles of dome growth, dome subsidence, degassing and explosive eruptions. Bull. Volcanol. 59, 72–82. https://doi.org/10.1007/s004450050176.

Matthews, S.J., Jones, A.P., Gardeweg, M.C., 1994. Lascar Volcano, Northern Chile; Evidence for Steady-State Disequilibrium. J. Petrol. 35, 401–432. https://doi.org/10.1093/petrology/35.2.401.

Matthews, S.J., Sparks, R.S., Gardeweg, M.C., 1999. The Piedras Grandes-Soncor eruptions, Lascar Volcano, Chile; Evolution of a Zoned Magma Chamber in the Central Andean Upper Crust. J. Petrol. 40, 1891–1919. https://doi.org/10.1093/petroj/40.12.1891.

Menard, G., Moune, S., Vlastélic, I., Aguilera, F., Valade, S., Bontemps, M., González, R., 2014. Gas and aerosol emissions from Lascar volcano (Northern Chile): Insights into the origin of gases and their links with the volcanic activity. J. Volcanol. Geoth. Res. 287, 51–67. https://doi.org/10.1016/j.jvolgeores.2014.09.004.

Milan, D.J., Heritage, G.L., Hetherington, D., 2007. Application of a 3D laser scanner in the assessment of erosion and deposition volumes and channel change in a proglacial river. Earth Surf. Process. Landf.: J. Brit. Geomorphol. Res. Grp. 32, 1657–1674. https://doi.org/10.1002/esp.1592.

Müller, D., Bredemeyer, S., Zorn, E., De Paolo, E., Walter, T.R., 2021. Surveying fumarole sites and hydrothermal alteration by unoccupied aircraft systems (UAS) at the La Fossa cone, Vulcano Island (Italy). J. Volcanol. Geoth. Res. 413, 107208 https://doi.org/10.1016/j.jvolgeores.2021.107208.

Oppenheimer, C., Francis, P.W., Rothery, D.A., Carlton, R.W., Glaze, L.S., 1993. Infrared image analysis of volcanic thermal features: Láscar Volcano, Chile, 1984–1992. J. Geophys. Res.: Solid Earth 98, 4269–4286. https://doi.org/10.1029/92JB02134.

Pavez, A., Remy, D., Bonvalot, S., Diament, M., Gabalda, G., Froger, J.L., Julien, P., Legrand, D., Moisset, D., 2006. Insight into ground deformations at Lascar volcano (Chile) from SAR interferometry, photogrammetry and GPS data: Implications on volcano dynamics and future space monitoring. Remote Sens. Environ. 100, 307–320. https://doi.org/10.1016/j.rse.2005.10.013.

Pritchard, M.E., Simons, M., 2002. A satellite geodetic survey of large-scale deformation of volcanic centres in the central Andes. Nature 418, 167–171. https://doi.org/10.1038/nature00872.

Pritchard, M.E., Simons, M., 2004. An InSAR-based survey of volcanic deformation in the central Andes. Geochem. Geophys. Geosyst. 5 https://doi.org/10.1029/2003GC000610.

Richter, N., Salzer, J.T., de Zeeuw-van Dalfsen, E., Perissin, D., Walter, T.R., 2018. Constraints on the geomorphological evolution of the nested summit craters of Láscar volcano from high spatio-temporal resolution TerraSAR-X interferometry. Bull. Volcanol. 80, 1–17. https://doi.org/10.1007/s00445-018-1195-3.

Robin, C., Camus, G., Gourgaud, A., 1991. Eruptive and magmatic cycles at Fuego de Colima volcano (Mexico). J. Volcanol. Geoth. Res. 45, 209–225. https://doi.org/10.1016/0377-0273(91)90060-D.

Roche, O., Druitt, T., Merle, O., 2000. Experimental study of caldera formation. J. Geophys. Res.: Solid Earth 105, 395–416. https://doi.org/10.1029/1999JB900298.

Roche, O., Van Wyk De Vries, B., Druitt, T.H., 2001. Sub-surface structures and collapse mechanisms of summit pit craters. J. Volcanol. Geoth. Res. 105, 1–18. https://doi.org/10.1016/S0377-0273(00)00248-1.

Sahetapy-Engel, S.T., Harris, A.J., 2009. Thermal structure and heat loss at the summit crater of an active lava dome. Bull. Volcanol. 71, 15–28. https://doi.org/10.1007/s00445-008-0204-3.

Salzer, J.T., Milillo, P., Varley, N., Perissin, D., Pantaleo, M., Walter, T.R., 2017. Evaluating links between deformation, topography and surface temperature at volcanic domes: Results from a multi-sensor study at Volcán de Colima, Mexico. Earth Planet. Sci. Lett. 479, 354–365. https://doi.org/10.1016/j.epsl.2017.09.027.

Schöpa, A., Pantaleo, M., Walter, T., 2011. Scale-dependent location of hydrothermal vents: Stress field models and infrared field observations on the Fossa Cone, Vulcano Island, Italy. J. Volcanol. Geoth. Res. 203, 133–145. https://doi.org/10.1016/j.jvolgeores.2011.03.008.

Spampinato, L., Calvari, S., Oppenheimer, C., Boschi, E., 2011. Volcano surveillance using infrared cameras. Earth Sci. Rev. 106, 63–91. https://doi.org/10.1016/j.earscirev.2011.01.003.

Sparks, R.S., Gardeweg, M.C., Calder, E.S., Matthews, S.J., 1997. Erosion by pyroclastic flows on Lascar Volcano, Chile. Bull. Volcanol. 58, 557–565. https://doi.org/10.1007/s004450050162.

Stern, C.R., 2004. Active Andean volcanism: its geologic and tectonic setting. Rev. Geol. Chile 31, 161–206. https://doi.org/10.4067/S0716-02082004000200001.

Stevenson, J.A., Varley, N., 2008. Fumarole monitoring with a handheld infrared camera: Volcán de Colima, Mexico, 2006–2007. J. Volcanol. Geoth. Res. 177, 911–924. https://doi.org/10.1016/j.jvolgeores.2008.07.003.

Taddeucci, J., Sottili, G., Palladino, D.M., Ventura, G., Scarlato, P., 2010. A note on maar eruption energetics: current models and their application. Bull. Volcanol. 72, 75–83. https://doi.org/10.1007/s00445-009-0298-2.

Tassi, F., Aguilera, F., Vaselli, O., Medina, E., Tedesco, D., Delgado Huertas, A., Poreda, R., Kojima, S., 2009. The magmatic- and hydrothermal-dominated fumarolic system at the Active Crater of Lascar volcano, northern Chile. Bull. Volcanol. 71, 171–183. https://doi.org/10.1007/s00445-008-0216-z.

Tibaldi, A., Corti, N., De Beni, E., Luca Bonali, F., Falsaperla, S., Langer, H., Neri, M., Cantarero, M., Reitano, D., Fallati, L., 2021. Mapping and evaluating kinematics and the stress and strain field at active faults and fissures: a comparison between field and drone data at the NE rift, Mt Etna (Italy). Solid Earth 12, 801–816. https://doi.org/10.5194/se-12-801-2021.

Turner, N.R., Perroy, R.L., Hon, K., 2017. Lava flow hazard prediction and monitoring with UAS: a case study from the 2014–2015 Pāhoa lava flow crisis, Hawai'i. J. Appl. Volcanol. 6, 1–11. https://doi.org/10.1186/s13617-017-0068-3.

Valentine, G.A., White, J.D., Ross, P.S., Amin, J., Taddeucci, J., Sonder, I., Johnson, P.J., 2012. Experimental craters formed by single and multiple buried explosions and implications for volcanic craters with emphasis on maars. Geophys. Res. Lett. 39 https://doi.org/10.1029/2012GL053716.

Walter, T.R., Belousov, A., Belousova, M., Kotenko, T., Auer, A., 2020. The 2019 Eruption Dynamics and Morphology at Ebeko Volcano Monitored by Unoccupied Aircraft Systems (UAS) and Field Stations. Remote Sens. 12 https://doi.org/10.3390/rs12121961.

Walter, T.R., Zorn, E.U., Harnett, C.E., Shevchenko, A.V., Belousov, A., Belousova, M., Vassileva, M.S., 2022. Influence of conduit and topography complexity on spine extrusion at shiveluch volcano, kamchatka. Commun. Earth Environ. 3, 1–10. https://doi.org/10.1038/s43247-022-00491-w.

Westoby, M.J., Brasington, J., Glasser, N.F., Hambrey, M.J., Reynolds, J.M., 2012. 'Structure-from-Motion' photogrammetry: A low-cost, effective tool for geoscience applications. Geomorphology 179, 300–314. https://doi.org/10.1016/j.geomorph.2012.08.021.

Wheaton, J.M., Brasington, J., Darby, S.E., Sear, D.A., 2010. Accounting for uncertainty in DEMs from repeat topographic surveys: Improved sediment budgets. Earth Surf. Proc. Land. 35, 136–156. https://doi.org/10.1002/esp.1886.

Whelley, P.L., Jay, J., Calder, E.S., Pritchard, M.E., Cassidy, N.J., Alcaraz, S., Pavez, A., 2012. Post-depositional fracturing and subsidence of pumice flow deposits: Lascar Volcano, Chile. Bull. Volcanol. 74, 511–531. https://doi.org/10.1007/s00445-011-0545-1.

Wooster, M.J., 2001. Long-term infrared surveillance of Lascar Volcano: Contrasting activity cycles and cooling pyroclastics. Geophys. Res. Lett. 28, 847–850. https://doi.org/10.1029/2000GL011904.

Wooster, M.J., Rothery, D.A., 1997. Thermal monitoring of Lascar Volcano, Chile, using infrared data from the along-track scanning radiometer: a 1992–1995 time series. Bull. Volcanol. 58, 566–579. https://doi.org/10.1007/s004450050163.

Zimmer, M., Walter, T.R., Kujawa, C., Gaete, A., Franco-Marin, L., 2017. Thermal and gas dynamic investigations at Lastarria volcano, Northern Chile. The influence of precipitation and atmospheric pressure on the fumarole temperature and the gas velocity. J. Volcanol. Geoth. Res. 346, 134–140. https://doi.org/10.1016/j.jvolgeores.2017.03.013.

Zorn, E.U., Walter, T.R., Heap, M.J., Kueppers, U., 2020. Insights into lava dome and spine extrusion using analogue sandbox experiments. Earth Planet. Sci. Lett. 551, 116571 https://doi.org/10.1016/j.epsl.2020.116571.